Nanoscale

Elucidating the Surface Compositions of Pd@Pt_{nL} Core-Shell Nanocrystals through Catalytic Reactions and Spectroscopy Probes

Journal:	*Nanoscale*
Manuscript ID	NR-ART-08-2021-005636.R1
Article Type:	Paper
Date Submitted by the Author:	07-Oct-2021
Complete List of Authors:	Zhai, Peng; Louisiana State University, Cain Department of Chemical Engineering Shi, Yifeng; Georgia Institute of Technology, Wang, Qiuxiang; Georgia Institute of Technology Xia, Younan; Georgia Institute of Technology, The Wallace H. Coulter Department of Biomedical Engineering Ding, Kunlun; Louisiana State University and A&M College,

Elucidating the Surface Compositions of Pd@Pt_{nL} Core-Shell Nanocrystals through Catalytic Reactions and Spectroscopy Probes

Peng Zhai,[a†] Yifeng Shi,[b†] Qiuxiang Wang,[c] Younan Xia,[*b,c,d] and Kunlun Ding[*a]

[a]Department of Chemical Engineering, Louisiana State University, Baton Rouge, Louisiana 70803, USA. E-mail: kunlunding@lsu.edu (for catalytic measurements and spectra characterization)

[b]School of Chemical and Biomolecular Engineering, Georgia Institute of Technology, Atlanta, Georgia 30332, USA. E-mail: younan.xia@bme.gatech.edu (for material synthesis and electron microscope characterization)

[c]The Wallace H. Coulter Department of Biomedical Engineering, Georgia Institute of Technology and Emory University, Atlanta, Georgia 30332, USA

[d]School of Chemistry and Biochemistry, Georgia Institute of Technology, Atlanta, Georgia 30332, USA

Abstract

The catalytic behaviors or properties of bimetallic catalysts are highly dependent on the surface composition, but it has been a grand challenge to acquire such information. In this work, we employ Pd@Pt_{nL} core-shell nanocrystals with an octahedral shape and tunable Pt shell thickness as a model system to elucidate their surface compositions using catalytic reactions based upon the selective hydrogenation of butadiene and acetylene. Our results indicate that the surface of the core-shell nanocrystals changed from Pt-rich to Pd-rich when they were subjected to calcination under oxygen, a critical step involved in the preparation of many industrial catalysts. The inside-out migration can be attributed to both atomic interdiffusion and the oxidation of Pd atoms during the calcination process. The changes in surface composition were further confirmed using infrared and X-ray photoelectron spectroscopy. This work offers insightful guidance for the development and optimization of bimetallic catalysts toward various reactions.

Introduction

Since the pioneering work by Sinfelt in 1970s,[1] bimetallic nanoparticles have received ever-increasing interest in heterogeneous catalysis.[2,3] They usually exhibit superior performance over their monometallic counterparts as a result of the synergies between the constituent metals, which may arise from a combination of ensemble, ligand, and geometric effects.[4-6] When describing the properties of a bimetallic system, one needs additional information other than its gross elemental composition. At the same elemental ratio, the nanoparticle can still display very different surface compositions and thus distinct catalytic properties depending on how the two metals are spatially distributed across the particle. For example, in addition to the dispersion of one metal as phase-segregated domains in the matrix of another metal, the two metals can take other configurations, including the formation of homogeneous alloy, intermetallic, and core-shell structures.[7,8] During the preparation, pretreatment, and operation of a bimetallic catalyst, the surface composition may undergo dynamic changes, making it extremely challenging to elucidate the active sites, understand the catalytic mechanism, and establish the composition-structure-property relationship.[9,10]

The present work focuses on bimetallic nanocrystals initially prepared with a well-defined core-shell structure. Such nanocrystals offer the capability to enhance the catalytic performance of surface atoms by introducing charge transfer and lattice strain while promising an avenue to reduce the overall cost of a catalyst by adding an earth abundant and inexpensive metal to the core.[11-14] Despite recent advancement in their colloidal synthesis, it remains a daunting task to understand their catalytic properties due to the possible intermixing between the atoms in the core and shell

and thus dynamic changes to the surface composition. What is worse, such a thermodynamically favored process is often accelerated during the operation of a catalyst or even when the catalyst is subjected to a pretreatment process that involves heating and/or exposure to a reactive gas.[15-19] As a matter of fact, surface reconfiguration in terms of composition is commonly observed during the thermal annealing of core-shell nanoparticles.[20,21] In a recent study, for example, we used scanning transmission electron microscopy (STEM) with *in situ* heating capability to monitor the thermal stability of Pd@Pt_{4L} nanocrystals in real time.[21] For the nanocrystal with a cubic shape, it was found that the core-shell structure could be retained up to 700 °C. In contrast, the core and shell of an octahedral nanocrystal went through significant alloying when annealed at 600 °C for 20 min. In another example, *in situ* transmission electron microscopy (TEM) and X-ray photoelectron spectroscopy (XPS) were applied to understand the change in surface composition of Ni@Co nanoparticles.[20] As the temperature for annealing was increased, the bimetallic nanoparticles went through a series of structural changes, including oxide removal, metal segregation, and alloy formation. It is worth noting that these two studies were carried out under vacuum without the involvement of a reactive gas. Surface restructuring is expected to become more dynamic and complicated under real catalytic conditions.[9]

In order to understand the catalytic behaviors or properties of bimetallic core-shell nanocrystals, it is essential to have a precise knowledge of their surface compositions. Electron microscopy and surface-sensitive spectroscopy are the tools typically used to accomplish this goal. Specifically, aberration-corrected STEM allows one to resolve the surface composition based on the differences in lattice spacing and Z-contrast.[21] Ambient-pressure, synchrotron-based XPS with

tunable X-ray energies has also been used to reveal changes to the surface atomic fraction when bimetallic nanocrystals were subjected to thermal annealing and/or different atmospheres.[22] Furthermore, infrared (IR) spectroscopy has long been employed, with certain probe molecules such as CO, to analyze the surface composition of bimetallic catalysts. In one of our recent studies, we successfully distinguished the Pt- and Pd-terminated surfaces of two different types of Pd-Pt bimetallic nanoparticles prepared using co-adsorption and sequential adsorption, respectively.[23]

With a focus on Pd@Pt_{nL} nanocrystals featuring a well-defined shape and Pt shell thickness, here we report the use of catalytic reactions and spectroscopy methods to determine their surface compositions. Such core-shell nanocrystals can be reliably synthesized using a colloidal method and have been actively explored as electrocatalysts toward the oxygen reduction reaction involved in the operation of fuel cells.[24] According to theoretical calculations, however, the higher surface energy of Pt relative to that of Pd made the Pd@Pt core-shell structure less stable than Pt@Pd core-shell structure and Pd-Pt alloy.[25] In an attempt to understand their behaviors under catalytic conditions, we use the selective hydrogenation of butadiene and acetylene to elucidate their surface compositions. We choose these two reactions as the probes because Pd and Pt exhibit distinct intrinsic activity and selectivity toward these reactions. Any changes in surface composition should be reflected by the catalytic activity and selectivity. With and without calcination in oxygen at 400 ^{o}C, the bimetallic nanocrystals indeed behave differently toward the selective hydrogenation of butadiene and acetylene. The origin of these differences in catalysis was further investigated using CO-based IR spectroscopy, XPS, and aberration-corrected STEM. Collectively, our results confirm that the surface of the core-shell nanocrystals change from Pt-rich to Pd-rich during

calcination under oxygen, shedding light on the future development of bimetallic catalysts toward various reactions.

Experimental Section

Chemicals and Materials

Poly(vinyl pyrrolidone) (PVP, with an average molecular weight of 55,000), L-ascorbic acid (AA, BioXtra, 99%), potassium bromide (KBr, 99.9%), citric acid (CA, 99.5%), formaldehyde solution (HCHO, 36.5−38% in H_2O), benzyl ether (BE, 98%), oleylamine (OAm, 70%), oleic acid (OA, 90%), manganese carbonyl ($Mn_2(CO)_{10}$, 98%), platinum(II) acetylacetonate ($Pt(acac)_2$, 97%), poly(ethylene oxide) (with an average molecular weight of 100,000), and tetraethyl orthosilicate (98%) were all purchased from Sigma-Aldrich. Chloroform (biotechnology grade) was ordered from AMERSCO. Sodium tetrachloropalladate(II) (Na_2PdCl_4, 36%Pd) was obtained from Acros Organics. All aqueous solutions were prepared using deionized (DI) water with a resistivity of 18.2 MΩ·cm at room temperature.

Synthesis of Pd Nanocubes

The Pd cubes with an average edge length of 10 nm were prepared by following a previously reported protocol.[26] In a typical synthesis, 105 mg of PVP, 60 mg of AA, and 300 mg of KBr were dissolved in 8 mL of water hosted in a glass vial. The vial was preheated in an oil bath held at 80 °C under magnetic stirring. After preheating for 10 min, 3 mL of aqueous Na_2PdCl_4 solution (19 mg mL^{-1}) was added in one shot. The reaction was allowed to proceed at 80 °C for 3 h. The solid products were collected through centrifugation, washed three times with water, and re-dispersed in water for seed-mediated growth.

Synthesis of Pd Octahedral Nanocrystals

The Pd octahedra with an average edge length of 20 nm were synthesized using seed-mediated growth.[27] Typically, 8 mL of an aqueous mixture containing 105 mg of PVP, 100 μL of HCHO, and 0.54 mg of the 10-nm Pd cubes was preheated at 60 °C under magnetic stirring. After 10 min, 3 mL of an aqueous solution containing 29 mg of Na_2PdCl_4 was injected in one-shot and the

reaction mixture was kept at 60 °C for 3 h. The solid products were collected through centrifugation, washed twice with water, and re-dispersed in water.

Synthesis of Pt Octahedral Nanocrystals

The Pt octahedra with an average edge length of 13 nm were prepared by following a previously published protocol.[28] In a typical synthesis, a mixture containing 80 mg of $Pt(acac)_2$, 10 mL of BE, 7.36 mL of OAm, and 1.25 mL of OA was preheated at 160 °C under Ar atmosphere, followed by the injection of 1 mL of chloroform containing 8 mg of $Mn_2(CO)_{10}$. The reaction mixture was held at 230 °C for 30 min. The solid products were collected by centrifugation, washed with ethanol, and were re-dispersed in hexane or acetone.

Synthesis of Pd@Pt Octahedral Nanocrystals with Different Shell Thicknesses

The $Pd@Pt_{0.85L}$ and $Pd@Pt_{3.1L}$ octahedral nanocrystals were synthesized in an aqueous solution by modifying a previously reported protocol,[29] For the synthesis of $Pd@Pt_{0.85L}$, 9 mL of an aqueous mixture containing 35 mg of PVP, 4 mg of CA, 0.5 mg of the 20-nm Pd octahedra was heated at 95 °C for 10 min, followed by the injection of 3 mL of aqueous K_2PtCl_4 solution (0.66 mg mL^{-1}). The reaction mixture was kept at 95 °C for 6 h. For the synthesis of $Pd@Pt_{3.1L}$, 9 mL of an aqueous mixture containing 100 mg of PVP, 30 mg of CA, 0.5 mg of the 20-nm Pd octahedra was heated at 95 °C for 10 min, followed by the injection of 3 mL of aqueous K_2PtCl_4 solution (10 mg mL^{-1}). The reaction mixture was kept at 95 °C for 12 h. The solid products were collected by centrifugation, washed twice with water, and finally re-dispersed in water.

Support Preparation and Catalyst Loading

The mesoporous-SiO_2 support was prepared using a sol-gel process according to the literature.[30] Typically, 44 g of poly(ethylene oxide) was dissolved in 440 g of 1 M HNO_3 in a VWR KIMAX Media/Storage glass bottle (1 L) at room temperature. After the introduction of 286 g of tetraethyl orthosilicate, the solution was sealed and stirred on a stir plate at room temperature for 30 min. The bottle was then transferred to an oven preheated to 40 °C and kept there for 2.5 days. The resultant monolithic white gel was broken into small pieces (< 5 mm) and immersed in 300 mL of water to leach out the acid remaining in the gel. The solvent was changed every 2 hours. The 4th

solvent was 0.045 M aqueous NH_4OH. The bottle was sealed and kept in the oven held at 40 °C for 24 h. The gel particles were then rinsed with water and dried at 40 °C for 24 h and at 100 °C for 12 h. The dried gel particles were calcined in air with a temperature ramping rate of 1.5 °C min^{-1} up to 600 °C and then kept at this temperature for 12 h. The specific surface area of the as-obtained SiO_2 was *ca*. 1000 m^2 g^{-1}, with a total pore volume of 5 mL g^{-1}, including macropores, mesopores, and micropores.[30]

The loadings of Pd/Pt were fixed at 1 wt.% on SiO_2 using adsorption method (for Pd@Pt bimetallic samples, the total loading of Pd and Pt was 1 wt.%). Typically, 200 mg of mesoporous SiO_2 powders were dispersed in 5 mL of H_2O by sonication. Then, 2 mL of the colloidal suspension of nanocrystals (0.5 mg mL^{-1}, measured by inductively-coupled plasma mass spectrometry, ICP-MS) was added dropwise under vigorous agitation. The mixture was sonicated for 10 min to remove bubbles or aggregates. The nanocrystals were deposited on the support after centrifugation at 5,000 rpm for 1 min. The solid was washed three times with water, twice with a mixture of water and acetone (1:3, v/v), and twice with acetone. For Pt nanocrystals, the loading was conducted in toluene, and the solid was washed three times with toluene and twice with pentane. The as-obtained solid products were dried at room temperature overnight.

Catalytic Activity Evaluation

The selective hydrogenation was conducted in a fixed bed using a 1/4 inch quartz reactor. The gas stream at the reactor outlet was analyzed using online Agilent 490 microGC equipped with MS-5A (H_2, N_2, CH_4, CO), Plot U (CO_2, C_2H_2, C_2H_4, and C_2H_6), and Alumina (C_{3+} alkanes and C_{3+} alkenes, butadiene) columns. Each column was connected to a separated thermal conductivity detector. N_2 was used as an internal standard for gas chromatography (GC) quantification.

For butadiene hydrogenation, 10 mg of catalyst was diluted with 400 mg of quartz sand. The pretreatment conditions were kept the same as what were used the acetylene hydrogenation. The reaction gas mixture was C_4H_6:H_2:N_2 = 2: 4: 114 mL min^{-1}. After switched from N_2 to reaction gas, reaction temperature was increased from 20 °C to 180 °C with a ramp rate of 1 °C min^{-1}.

For C_2H_2/C_3H_6 competitive hydrogenation, 20 mg of catalyst was diluted with 400 mg of quartz sand. For non-calcined catalysts, they were reduced in 10% H_2/N_2 at 100 °C for 30 min before reaction. For calcined catalysts, they were pretreated with 10% O_2/N_2 at 400 °C for 30 min

and then reduced by 10% H_2/N_2 at 100 °C for 30 min. This calcination condition was chosen to remove the PVP employed in the synthesis since the PVP is known to decompose near 400 °C.[31] Propylene was co-fed with acetylene at a ratio of C_2H_2:H_2:C_3H_6:N_2 = 0.75: 1.5: 15: 57.75 mL min^{-1}. The gas flow rates were controlled by mass flow controllers (MKS Instruments). After switched from N_2 to reaction gas, reaction temperature was increased from 40 °C to 180 °C at a ramp rate of 2 °C min^{-1}.

Instrumentation

Transmission electron microscopy images were taken using Hitachi HT-7700 at an acceleration voltage of 120 kV. High-angle annular dark-field scanning transmission electron microscopy (HAADF-STEM) images and energy-dispersive X-ray spectroscopy (EDX) mapping were obtained using a Hitachi HD2700 aberration-corrected microscope operated at 200 kV. The samples were prepared by drop-casting the nanoparticle dispersion on carbon-coated copper grids and dried at room temperature. The concentrations of Pd and Pt in colloidal solutions were determined using an ICP-MS (NexION 300Q, PerkinElmer). X-ray photoelectron spectroscopy was carried out on Kratos AXIS 165 XPS/AES. The binding energies were calibrated by fixing the Si 2p peak at 103.4 eV. We measured the freshly prepared Pd@Pt/SiO_2 samples before and after calcination under 10%O_2/N_2 at 400 °C for 30 min. Diffuse reflectance infrared Fourier transform spectroscopy (DRIFTS) measurements were conducted on a Thermo Nicolet 6700 instrument with a Hg-Cd-Te (MCT) detector. The SiO_2-supported samples were placed in a Praying Mantis high temperature reaction cell with KBr windows. The non-calcined samples were reduced with 100 mL min^{-1} of 10% H_2/Ar at 100 °C for 30 min. For the calcined samples, they were pretreated with 10% O_2/N_2 at 400 °C for 30 min and then reduced by 10% H_2/N_2 at 100 °C for 30 min. After treatment, the samples were cooled down to record the background in 100 mL min^{-1} He flow. The CO adsorption was performed at room temperature by introducing 5% CO/Ar into the DRIFTS cell at a flow rate of 100 mL min^{-1}. After CO saturation (15 min), He gas at a flow rate of 100 mL min^{-1} was introduced to remove gas phase CO from the catalyst. The spectra presented in this paper were collected after desorption in He for 15 min. All the spectra were recorded using 32 scans at a resolution of 4 cm^{-1}.

Results and Discussion

Figure 1a shows the synthesis of Pd@Pt core-shell nanocrystals by conformally depositing Pt atoms on Pd octahedral seeds of 20 nm in edge length (Figure S1a). The thickness of the Pt shell can be tuned by controlling the amount of the Pt(II) precursor added into the reaction mixture, the amount of the reducing agent, the reaction time, or a combination of these parameters. Once synthesized, the average thickness of the Pt shell on each particle could be derived from the metal contents determined using ICP-MS. Specifically, we focused on the two samples shown in Figure 1, b-e, denoted Pd@$Pt_{0.85L}$ and Pd@$Pt_{3.1L}$, respectively, where the average thicknesses of their Pt shells were 0.85 and 3.1 atomic layers. Figure 1, c and e, shows atomic-resolution HAADF-STEM images of individual particles taken from these samples. For Pd@$Pt_{0.85L}$, the total number of Pt atoms was inadequate to cover the entire surface of the Pd octahedral seed. Therefore, only a partial Pt shell could be identified on the surface of the particle based on the difference in contrast between Pd and Pt. When the thickness was increased to 3.1 atomic layers, a complete, well-defined Pt shell was resolved around the particle. The small bumps on the Pd@$Pt_{3.1L}$ were from the fusion of small particles, attributed to self-nucleation of Pt, on the octahedral surface during the synthesis. We also prepared Pt octahedra of 13 nm in edge length (Figure S1b). The Pt and Pd octahedral nanocrystals served as reference samples for both the catalytic and spectroscopy studies.

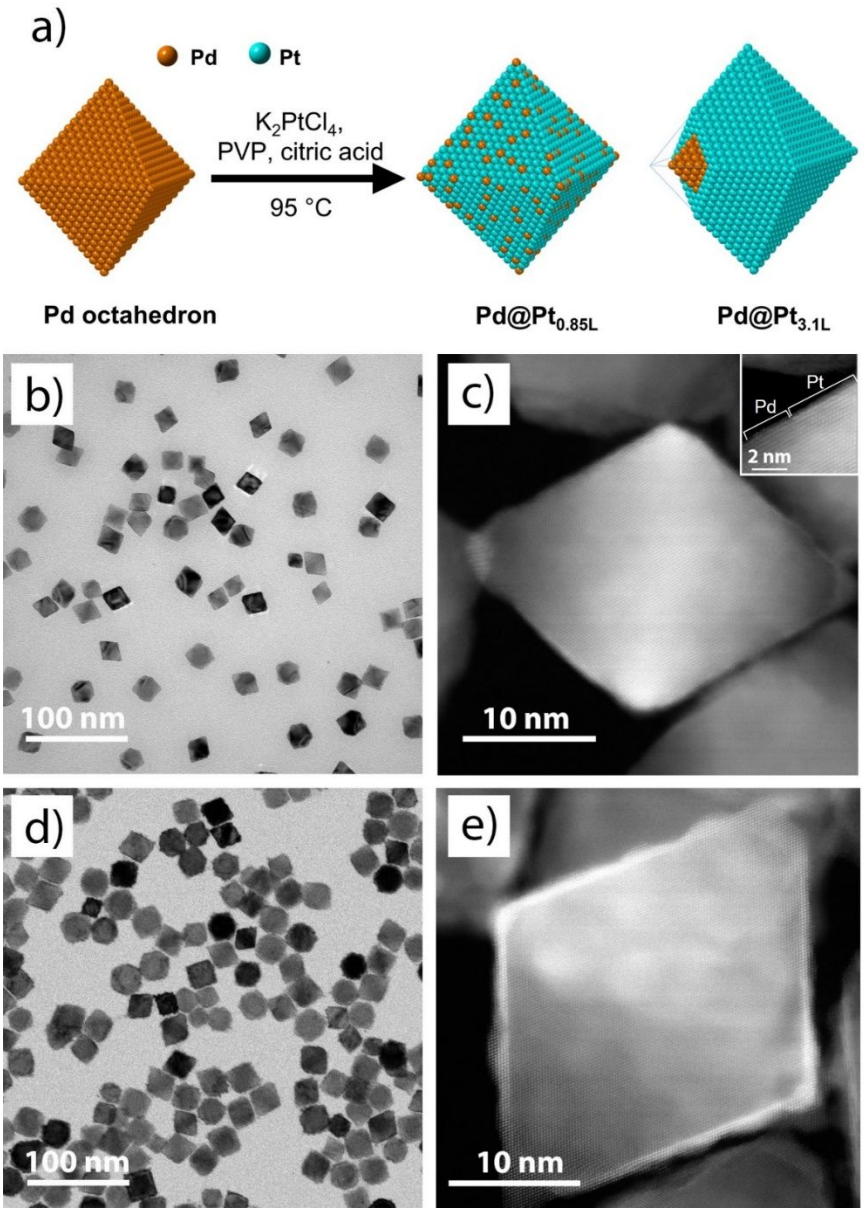

Figure 1. (a) Schematic illustration showing the synthesis of $Pd@Pt_{nL}$ octahedra *via* seed-mediated growth. (b, d) TEM and (c, e) HAADF-STEM images of (b, c) $Pd@Pt_{0.85L}$ octahedra and (d, e) $Pd@Pt_{3.1L}$ octahedra, respectively.

The nanocrystals were supported on mesoporous SiO_2 and tested as model catalysts toward the selective hydrogenation of butadiene and acetylene (see the experimental section for details). Figure 2a compares the results on butadiene hydrogenation, where the catalysts only went through reduction in H_2 at 100 ˚C for 30 min without involving calcination. The catalysts showed distinct activities, which decreased in the order of Pd > Pd@$Pt_{0.85L}$ > Pd@$Pt_{3.1L}$ > Pt. This trend confirms the blockage of Pd surface by the intrinsically less active Pt atoms. Since the Pd@$Pt_{3.1L}$ sample showed a much higher activity compared to its monometallic Pt counterpart, we argue that some Pd atoms were able to migrate all the way from the Pd core to the outer surface during the synthesis, reduction treatment, and/or hydrogenation reaction. Among these catalysts, those whose surfaces were dominated by Pd exhibited negligible selectivity toward butane at low conversion, while it was slightly increased at high conversion (Figure S2). Such a change in product selectivity can be explained by the site competition between butadiene hydrogenation and butene hydrogenation, which is sensitive to butadiene conversion.[32] In comparison, those dominated by Pt exhibited greater selectivity toward butane at low conversion.[33] As the Pt shells on Pd nanocrystals became thicker, the catalytic selectivity toward butane increased and appeared more “Pt-like” (Figure S2).

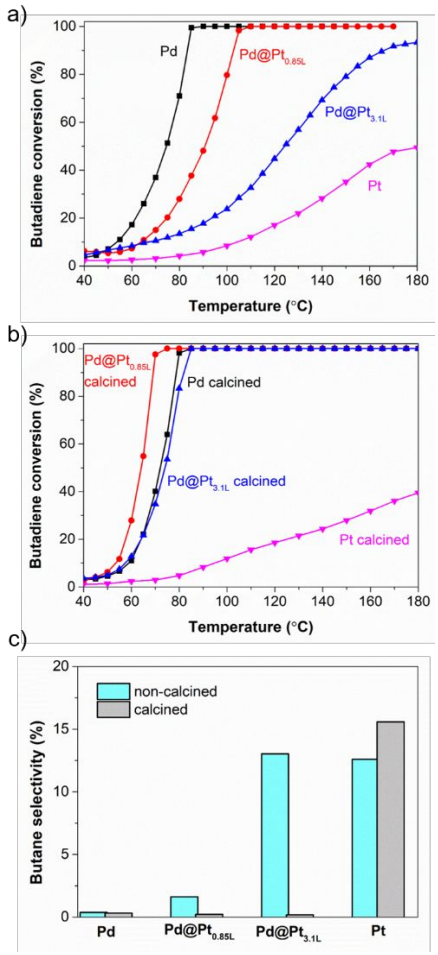

Figure 2. Hydrogenation of butadiene over Pd, Pt, and Pd@Pt_{nL} bimetallic catalysts. (a) Butadiene conversion as a function of temperature on the non-calcined catalysts. (b) Butadiene conversion as a function of temperature on the calcined catalysts. (c) Selectivity toward butane at about 10% butadiene conversion. All the samples went through reduction under 10% H_2/N_2 at 100 ˚C prior to catalytic tests.

As for the catalysts involving calcination, there was no pronounced change to the catalytic performance for Pd and Pt monometallic nanocrystals, indicating that the reactions were largely

insensitive to the surface structure as calcination did cause alternations to the shape and thus facets of the catalytic particles (Figure S3). In sharp contrast, as shown in Figure 2, b and c, the activity and selectivity of the Pd@Pt_{nL} nanocrystals changed drastically when calcined in 10% O_2/N_2 at 400 °C for 30 min, followed by reduction in 10% H_2/N_2 prior to the catalytic test. Both the activity and selectivity of the calcined core-shell nanocrystals became "Pd-like", implying significant changes to the surface composition during the calcination process.

Similar catalytic behaviors were also observed for the hydrogenation of acetylene, which was carried out under competitive conditions, with the co-feeding of a large excess of propylene (Figure 3). For the non-calcined catalysts, the Pd octahedra showed the best catalytic performance as it achieved complete conversion of acetylene at 160 °C, together with alkane selectivity below 5%. Both values are comparable with the best Pd-based catalyst reported in the literature.[34,35] The superb performance can be attributed to the relatively large particle size and thus small proportion of under-coordinated sites (*i.e.*, edges and corners) that are believed to be responsible for the strong adsorption of alkenes and thereby over-hydrogenation of alkynes to alkanes.[36] In comparison, the Pt octahedra showed much lower catalytic activity even at 180 °C, implying that Pt surface is significantly less active than Pd in catalyzing this reaction. As expected, the catalysts based on Pd@$Pt_{0.85L}$ and Pd@$Pt_{3.1L}$ exhibited intermediate activities between Pd and Pt octahedra, and the activity decreased as the average thickness of the Pt shells was increased. Meanwhile, the alkane selectivity on both the core-shell samples was much greater than that on the Pd sample. Similar to the trends observed in butadiene hydrogenation, the acetylene conversion of the calcined core-shell nanocrystals increased relative to the non-calcined ones, implying that surface reconstruction took place during the calcination process. However, the calcined bimetallic catalysts still show greater alkane selectivity compared to monometallic Pd catalyst, implying that their surfaces are not solely covered by Pd. As for butadiene hydrogenation, both Pd@Pt_{nL} samples after calcination exhibited almost the same performance as the monometallic Pd counterpart, indicating that the residue Pt on the surface should not contribute significantly to butadiene hydrogenation.

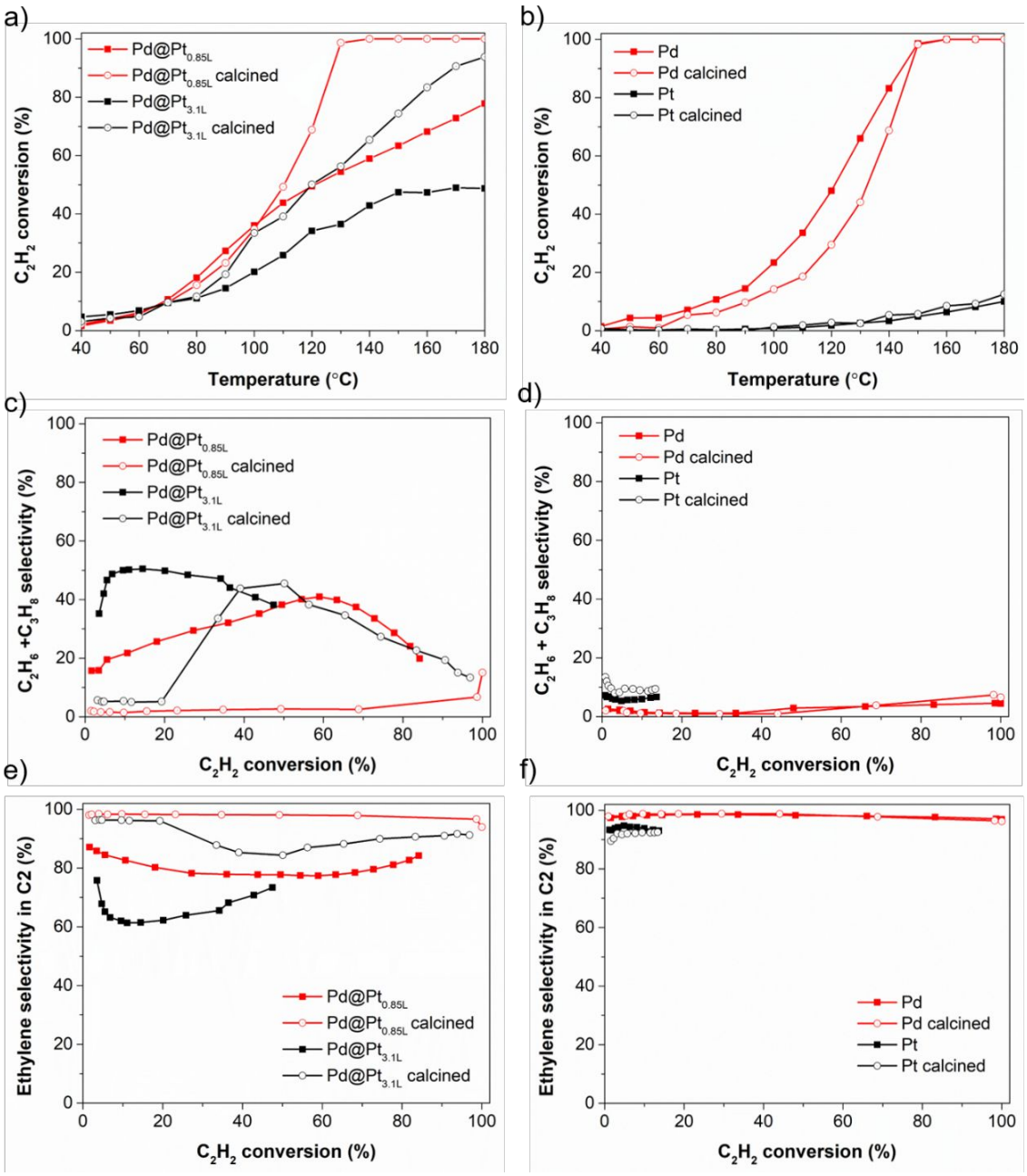

Figure 3. Selective hydrogenation of acetylene over Pd, Pt, and Pd@Pt_{nL} bimetallic catalysts. (a, b) Acetylene conversion as a function of temperature over (a) Pd@Pt_{nL} bimetallic catalysts and (b) Pd or Pt catalysts, respectively. (c, d) Alkane selectivity as a function of acetylene conversion over (c) Pd@Pt_{nL} bimetallic catalysts and (d) Pd or Pt catalysts, respectively. (e, f) Ethylene selectivity

as a function of acetylene conversion over (e) Pd@Pt_{nL} bimetallic catalysts and (f) Pd or Pt catalysts, respectively. All catalysts were reduced at 100 ˚C in 10% H_2/N_2 prior to catalytic tests.

For both the butadiene and acetylene hydrogenation reactions, the catalytic property of the Pd@Pt_{nL} nanocrystals switched from "Pt-like" to "Pd-like" upon calcination. The switching can be attributed to the outward migration of Pd atoms and thus increase in surface coverage by Pd atoms. Such a calcination-induced surface reconstruction was also supported by IR spectroscopy, with CO serving as a probe molecule. As a particularly powerful and versatile molecular probe to reveal the surface of metal catalysts, the vibrational frequency of CO is highly sensitive to the type of metal, oxidation state, and local coordination environment of the binding site.[37,38] For instance, CO molecules prefer to adsorb on a Pd surface in two-fold and three-fold bridge forms, while linear adsorption is the dominant mode on a Pt surface.[39] Figure 4 and Figure S4 show the infrared spectra of CO adsorbed on the calcined and non-calcined Pd, Pt, and Pd@Pt_{nL} nanocrystals at room temperature. Only one sharp bridge CO band (centered at 1983 cm^{-1}) was observed on the calcined Pd nanocrystals, without noticeable linear CO band in the region of 2000–2100 cm^{-1}.[40] In contrast, the calcined Pt nanocrystals showed a single sharp band at 2096 cm^{-1}, which can be assigned to linear CO adsorbed at well-coordinated Pt sites.[41] The narrow peak widths (full width at half maximum: 13 and 8 cm^{-1} for Pd and Pt, respectively) could be attributed to the uniform binding sites present on the calcined Pd and Pt nanocrystals.

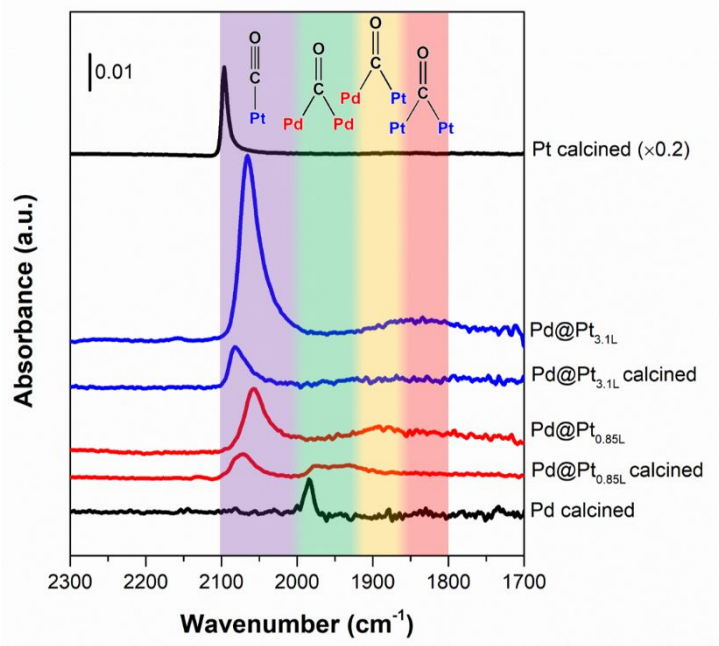

Figure 4. A comparison of the IR spectra of the CO adsorbed on Pd, Pt, and Pd@Pt_{nL} catalysts at room temperature. All catalysts were reduced at 100 ˚C in 10% H_2/N_2 prior to CO adsorption. Note that these spectra are differential spectra with individual background spectrum acquired in helium atmosphere prior to CO adsorption.

The bimetallic samples, on the other hand, exhibited features different from the monometallic samples. For the non-calcined Pd@$Pt_{0.85L}$ sample, a linear CO band (2058 cm^{-1}) and a bridge CO band (1900 cm^{-1}) appeared. The linear CO band could be attributed to the presence of Pt atoms on the surface since this band was absent in pure Pd sample. Given the fact that bridge CO bands on Pd and Pt surfaces usually appear at 1920−2000 cm^{-1} and 1800−1850 cm^{-1}, respectively, the band observed at 1900 cm^{-1} could be assigned to CO molecules adsorbed in a bridge form between one Pd atom and one Pt atom. As for the non-calcined Pd@$Pt_{3.1L}$ sample, the linear CO band became

even stronger. The bridge CO band centered at 1830 cm^{-1} clearly belongs to Pt atoms, while no characteristic Pd bridge band was observed. These data suggest that the surface of the non-calcined $Pd@Pt_{3.1L}$ nanocrystals was almost fully covered by Pt atoms. The calcined bimetallic samples exhibited blue-shifted and much weaker linear CO bands compared to the non-calcined samples. The blueshift likely originated from the removal of capping agent, poly(vinyl pyrrolidone), which could donate electrons to metals and thus weaken the CO bond. On the other hand, the Pt-Pt- or Pd-Pt-related bridge CO band either shifted to characteristic Pd-Pd bridge region or became too broad to be clearly resolved. These changes indicated that the surface coverage of Pt significantly decreased, though not completely diminished, upon calcination, which can be attributed to the migration of Pd atoms to the outmost surface.

Table 1. The Pt/Pd atomic ratio in the near-surface region of bimetallic samples quantified using XPS.

	Pt/Pd atomic ratio		
	non-calcined	calcined	calcined and reduced
$Pd@Pt_{0.85L}$	0.38	0.09	0.08
$Pd@Pt_{3.1L}$	1.27	0.70	0.81

We also carried out XPS analysis (Table 1 and Figure S5) to further support our argument and find out the possible cause of the Pd migration during sample calcination. The kinetic energies

of the escaping photoelectrons associated with Pd 3d and Pt 4f orbitals fall in the range of 1100–1400 eV, corresponding to an inelastic mean free path of 3–5 atomic layers. Therefore, the Pt/Pd atomic ratios listed in Table 1 represent the overall near-surface composition within 3–5 atomic layers of thickness. The XPS-derived Pt/Pd atomic ratios for the non-calcined Pd@$Pt_{0.85L}$ and Pd@$Pt_{3.1L}$ samples were 0.38 and 1.27, respectively, in good agreement with the analysis depth of XPS. These ratios dropped to 0.09 and 0.7, respectively, after calcination, indicating that Pd migrated into the near-surface region while a significant fraction of surface Pt diffused into the core region that was at least 3–5 atomic layers below the surface (Figure 5). More importantly, as shown in Figure S5, the introduction of oxygen during calcination would cause oxidation to the Pd atoms in the core, "pulling out" the Pd atoms to the surface in order to minimize the surface energy.[42] The XPS data not only confirmed the IR and catalytic data presented earlier, but also provide deeper insight into the origin of such migration. Compared with the Pd@Pt_{4L} octahedra heated under vacuum in an HRTEM,[21] where the intermixing between the core and shell mainly arose from atomic diffusion, the present work indicates that the presence of oxygen during calcination would further accelerate the mixing process. As a matter of fact, by tuning the interaction between metal atoms and gas molecules, the gas environments can even become the dominant factor in determining the surface composition of a bimetallic nanocrystal. For example, in the case of Rh_xPd_{1-x} nanoparticles, the surface composition and its chemical state would undergo reversible changes when the reactant gases change from oxidizing ones to reducing ones. [43,44] We believe the conclusion drawn from this study can also be extended to our Pd@Pt system: with the

presence of oxygen, and a stronger interaction between Pd and O, the intermixing process should be accelerated compared to those heated under vacuum.

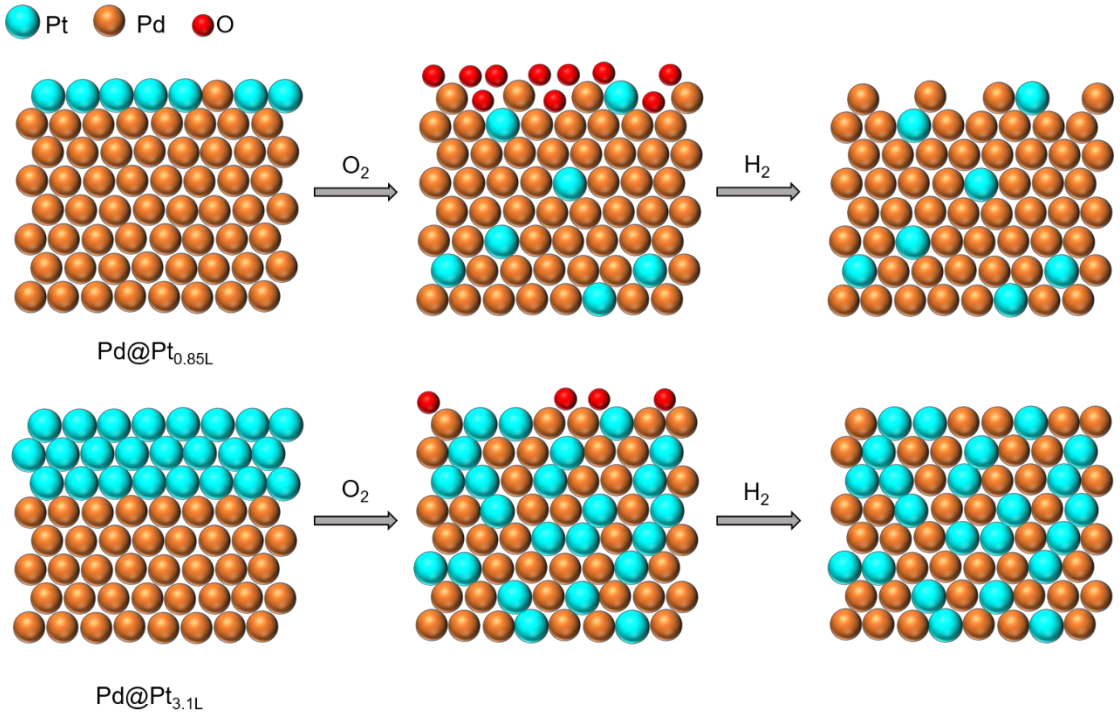

Figure 5. Schematic illustration showing near-surface restructurction of the Pd@Pt_{nL} nanocrystals during calcination and reduction.

Lastly, aberration-corrected STEM was also applied to directly visualize changes to both the surface composition and morphology upon calcination. Figure 6a shows a schematic illustration of the change in surface composition for both catalysts after calcination and reduction treatments. Compared with the calcined Pd octahedra shown in Figure S3, both Pd@$Pt_{0.85L}$ and Pd@$Pt_{3.1L}$ showed less significant deformation in shape during calcination, indicating the greater resistance of Pt toward thermal activation relative to Pd. Changes to the surface composition of the core-shell

nanocrystals can be identified from both the difference in contrast and EDX mapping. For the calcined Pd@$Pt_{0.85L}$ nanocrystal (Figure 6b), there was no longer a brighter Pt shell on the outmost layer of the particle. The composition distribution can be clearly identified in the insets of Figure 6b: only randomly scattered Pt atoms were observed within the nanocrystal. Some Pt atoms also aggregated on the surface of the nanocrystal, appeared as a brighter ring in the STEM image. In comparison to the as-synthesized Pd@$Pt_{0.85L}$, the corners of the octahedron were less sharp, indicating that shape deformation has taken place during the calcination treatment. For the Pd@$Pt_{3.1L}$ nanocrystal, both the octahedral shape and core-shell structure were largely retained during calcination. However, the Pt shell was partially broken during the calcination process, resulting in deformation to the well-defined {111} facet (Figure 6c) and intermixing between the Pd core and Pt shell (Figure S6). Although the shape of the Pd nanocrystals did not play a vital role in determining the catalytic activity and selectivity in this study, this observation has implication for the design of Pd-based catalysts toward structure-sensitive reactions. In principle, the shape stability of Pd nanocrystals could be improved by covering the surface with a Pt shell, albeit at the cost of incorporating some Pt atoms into the surface.

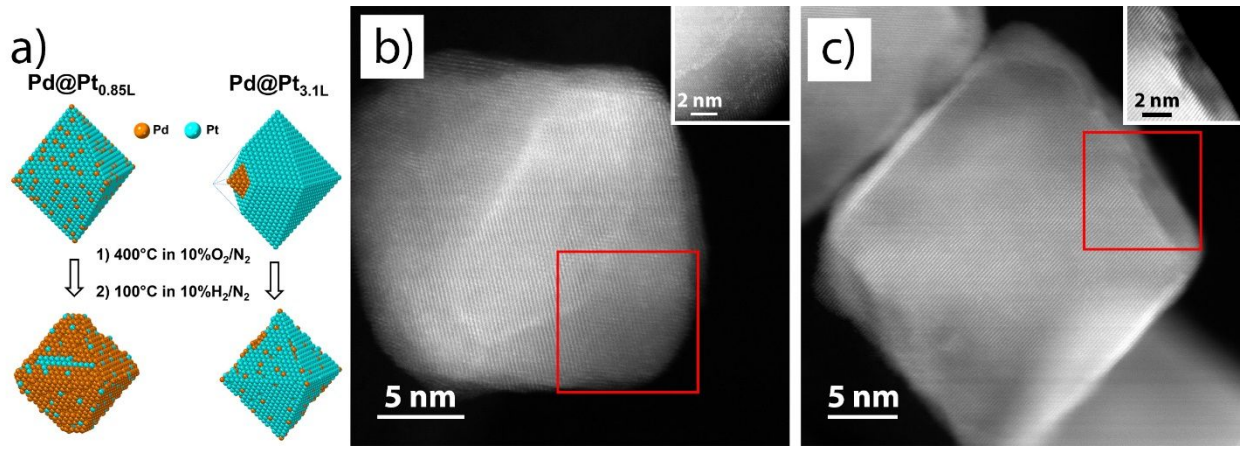

Figure 6. (a) Schematic illustration showing compositional and morphological changes to the $Pd@Pt_{nL}$ nanocrystals upon calcination in the presence of O_2. (b, c) HAADF-STEM images of the $Pd@Pt_{0.85L}$ and $Pd@Pt_{3.1L}$ nanocrystals, respectively, after calcination. The regions marked in red boxes in (b) and (c) are magnified at a higher resolution in their corresponding insets.

Conclusion

We have synthesized Pd, Pt, and Pd@Pt core-shell octahedral nanocrystals with different Pt shell thickness and further evaluated their catalytic behaviors. Two reaction probes (butadiene and acetylene hydrogenation) and two spectroscopy techniques (IR and XPS) were employed to shed light on the surface compositional dynamics typical of a bimetallic catalyst. Collectively, our results demonstrated that the surface composition of the core-shell nanocrystals would change from Pt-rich to Pd-rich when the sample was calcined in an oxidative atmosphere. The experimental approach should be extendible to the investigation of other types of core-shell

nanocrystals, providing guidance to the rational development of well-defined bimetallic catalysts with high activity and good selectivity toward various reactions.

Author Contributions

P. Zhai and Y. Shi contributed equally to this work.

Conflicts of Interest

The authors declare no conflict of interest.

Acknowledgement

This work was supported in part by start-up funds from Louisiana State University and the Georgia Institute of Technology. The electron microscopy analyses were conducted at the Georgia Tech Institute for Electronics and Nanotechnology, a member of the National Nanotechnology Coordinated Infrastructure (NNCI), which is supported by the National Science Foundation (ECCS-2025462). X-ray photoelectron spectroscopy was performed at the Shared Instrumentation Facility (SIF) at Louisiana State University.

References

1. J. H. Sinfelt, *Bimetallic Catalysts: Discoveries, Concepts, and Applications*, Wiley, 1983.

2. D. Wang and Y. Li, *Adv. Mater.*, 2011, **23**, 1044-1060.

3. M. Sankar, N. Dimitratos, P. J. Miedziak, P. P. Wells, C. J. Kiely and G. J. Hutchings, *Chem. Soc. Rev.*, 2012, **41**, 8099-8139.

4. M. Chen, D. Kumar, C. W. Yi and D. W. Goodman, *Science*, 2005, **310**, 291-293.

5. B. Lim, M. Jiang, P. H. Camargo, E. C. Cho, J. Tao, X. Lu, Y. Zhu and Y. Xia, *Science*, 2009, **324**, 1302-1305.

6. N. Agarwal, S. J. Freakley, R. U. McVicker, S. M. Althahban, N. Dimitratos, Q. He, D. J. Morgan, R. L. Jenkins, D. J. Willock, S. H. Taylor, C. J. Kiely and G. J. Hutchings, *Science*, 2017, **358**, 223-227.

7. K. D. Gilroy, A. Ruditskiy, H. C. Peng, D. Qin and Y. Xia, *Chem. Rev.*, 2016, **116**, 10414-10472.

8. Y. Pei, B. Zhang, R. V. Maligal-Ganesh, P. J. Naik, T. W. Goh, H. L. MacMurdo, Z. Qi, M. Chen, R. K. Behera, I. I. Slowing and W. Huang, *J. Catal.*, 2019, **374**, 136-142.

9. F. Tao, S. Zhang, L. Nguyen and X. Zhang, *Chem. Soc. Rev.*, 2012, **41**, 7980-7993.

10. H. Liao, A. Fisher and Z. J. Xu, *Small*, 2015, **11**, 3221-3246.

11. Y. Xia, Y. Xiong, B. Lim and S. E. Skrabalak, *Angew. Chem. Int. Ed.*, 2009, **48**, 60-103.

12. R. Ghosh Chaudhuri and S. Paria, *Chem. Rev.*, 2012, **112**, 2373-2433.

13. Y. Xia, K. D. Gilroy, H.-C. Peng and X. Xia, *Angew. Chem. Int. Ed.*, 2017, **56**, 60-95.

14. K. D. Gilroy, X. Yang, S. Xie, M. Zhao, D. Qin and Y. Xia, *Adv. Mater.*, 2018, **30**, 1706312.

15. K. J. Andersson, F. Calle-Vallejo, J. Rossmeisl and I. Chorkendorff, *J. Am. Chem. Soc.*, 2009, **131**, 2404-2407.

16. N. J. Divins, I. Angurell, C. Escudero, V. Pérez-Dieste and J. Llorca, *Science*, 2014, **346**, 620-623.

17. F. Calvo, *Phys. Chem. Chem. Phys.*, 2015, **17**, 27922-27939.

18. F. Gao, Y. Wang and D. W. Goodman, *J. Phys. Chem. C*, 2009, **113**, 14993-15000.

19. B. Zhu, G. Thrimurthulu, L. Delannoy, C. Louis, C. Mottet, J. Creuze, B. Legrand and H. Guesmi, *J. Catal.*, 2013, **308**, 272-281.

20. C. S. Bonifacio, S. Carenco, C. H. Wu, S. D. House, H. Bluhm and J. C. Yang, *Chem. Mater.*, 2015, **27**, 6960-6968.

21. M. Vara, L. T. Roling, X. Wang, A. O. Elnabawy, Z. D. Hood, M. Chi, M. Mavrikakis and Y. Xia, *ACS Nano*, 2017, **11**, 4571-4581.

22. F. F. Tao, L. Nguyen, S. Zhang, Y. Li, Y. Tang, L. Zhang, A. I. Frenkel, Y. Xia and M. Salmeron, *Nano Lett.*, 2016, **16**, 5001-5009.

23. K. Ding, D. A. Cullen, L. Zhang, Z. Cao, A. D. Roy, I. N. Ivanov and D. Cao, *Science*, 2018, **362**, 560-564.

24. H. Zhang, M. Jin and Y. Xia, *Chem. Soc. Rev.*, 2012, **41**, 8035-8049.

25. R. Huang, Y.-H. Wen, Z.-Z. Zhu and S.-G. Sun, *J. Phys. Chem. C*, 2012, **116**, 8664-8671.

26. M. Jin, H. Liu, H. Zhang, Z. Xie, J. Liu and Y. Xia, *Nano Res.*, 2011, **4**, 83-91.

27. M. Jin, H. Zhang, Z. Xie and Y. Xia, *Energy Environ. Sci.*, 2012, **5**, 6352-6357.

28. Y. Kang, J. B. Pyo, X. Ye, R. E. Diaz, T. R. Gordon, E. A. Stach and C. B. Murray, *ACS Nano*, 2013, **7**, 645-653.

29. J. Park, L. Zhang, S. I. Choi, L. T. Roling, N. Lu, J. A. Herron, S. Xie, J. Wang, M. J. Kim, M. Mavrikakis and Y. Xia, *ACS Nano*, 2015, **9**, 2635-2647.

30. K. Ding, A. Gulec, A. M. Johnson, T. L. Drake, W. Wu, Y. Lin, E. Weitz, L. D. Marks and P. C. Stair, *ACS Catal.*, 2016, **6**, 5740-5746.

31. K. M. Koczkur, S. Mourdikoudis, L. Polavarapu and S. E. Skrabalak, *Dalton Trans.*, 2015, **44**, 17883-17905.

32. J. Silvestre-Albero, G. Rupprechter and H.-J. Freund, *J. Catal.*, 2006, **240**, 58-65.

33. C. Yoon, M. X. Yang and G. A. Somorjai, *Catal. Lett.*, 1997, **46**, 37-41.

34. H. Zhou, X. Yang, L. Li, X. Liu, Y. Huang, X. Pan, A. Wang, J. Li and T. Zhang, *ACS Catal.*, 2016, **6**, 1054-1061.

35. F. Huang, Y. Deng, Y. Chen, X. Cai, M. Peng, Z. Jia, P. Ren, D. Xiao, X. Wen, N. Wang, H. Liu and D. Ma, *J. Am. Chem. Soc.*, 2018, **140**, 13142-13146.

36. M. Crespo-Quesada, A. Yarulin, M. Jin, Y. Xia and L. Kiwi-Minsker, *J. Am. Chem. Soc.*, 2011, **133**, 12787-12794.

37. C. Lamberti, A. Zecchina, E. Groppo and S. Bordiga, *Chem. Soc. Rev.*, 2010, **39**, 4951-5001.

38. K. Ding, A. Gulec, A. M. Johnson, N. M. Schweitzer, G. D. Stucky, L. D. Marks and P. C. Stair, *Science*, 2015, **350**, 189-192.

39. A. D. Allian, K. Takanabe, K. L. Fujdala, X. Hao, T. J. Truex, J. Cai, C. Buda, M. Neurock and E. Iglesia, *J. Am. Chem. Soc.*, 2011, **133**, 4498-4517.

40. E. Ozensoy, B. K. Min, A. K. Santra and D. W. Goodman, *J. Phys. Chem. B*, 2004, **108**, 4351-4357.

41. M. J. Kale and P. Christopher, *ACS Catal.*, 2016, **6**, 5599-5609.

42. H. Nie, J. Y. Howe, P. T. Lachkov and Y.-H. C. Chin, *ACS Catal.*, 2019, **9**, 5445-5461.

43. F. Tao, M. E. Grass, Y. Zhang, D. R. Butcher, F. Aksoy, S. Aloni, V. Altoe, S. Alayoglu, J. R. Renzas, C.-K. Tsung, Z. Zhu, Z. Liu, M. Salmeron and G. A. Somorjai, *J. Am. Chem. Soc.*, 2010, **132**, 8697-8703.

44. L.-L. Wang, T. L. Tan and D. D. Johnson, *Nano Lett.*, 2014, **14**, 7077-7084.